High irradiance performance of metal halide perovskites for concentrator photovoltaics

Zhiping Wang,† Qianqian Lin,† Bernard Wenger, M. Greyson Christoforo, Yen-Hung Lin, Matthew T. Klug, Michael B. Johnston, Laura M. Herz, Henry J. Snaith*
Clarendon Laboratory, Department of Physics, University of Oxford, Parks Road, Oxford, OX1 3PU, United Kingdom
**Correspondence:* henry.snaith@physics.ox.ac.uk

Abstract
Traditionally, III-V multi-junction cells have been employed in concentrator photovoltaic (CPV) applications, which deliver extremely high efficiencies, but have failed to compete with "flat plate" silicon technologies due to cost. Here, we assess the feasibility of employing metal-halide perovskites for CPVs and evaluate their device performance and stability under concentrated light. Under simulated sunlight, we achieve a peak efficiency of 23.6 % under 14 suns (that is, 14 times the standard solar irradiance), as compared to 21.1 % under 1 sun, and measure 1.26 V open-circuit voltage under 53 suns, for a material with a band gap of 1.63 eV. Importantly, our encapsulated devices maintain over 90% of their original efficiency after 150 h aging under 10 suns at maximum power point. Our work reveals the potential of perovskite CPVs, and may lead to new PV deployment strategies combining perovskites with low-concentration factor and lower accuracy solar tracking systems.

Introduction

For mainstream utility-scale PV, the module cost has dropped to less than half the cost of the total PV installation. This makes strategies that raise the module efficiency increasingly important, since an increased power output per m^2 of deployed PV offsets the balance of systems costs, which predominantly scale with area. The economic pressure to deliver higher power output per m^2, are also making more expensive deployment strategies feasible, such as solar tracking for flat-plate technologies[1,2]. As the fraction of global electricity generation from PV increases, it will become increasingly important to spread the temporal profile for PV electricity generation as broadly as possible throughout the day. With the latter consideration, 2-axis solar tracking, where the PV modules point directly towards the sun from dawn to dusk, should become increasingly popular. If we anticipate that sensible 2-axis solar tracking strategies will be developed and become economically viable through manufacturing and deployment

scaling, we should consider high efficiency PV concepts which work best under direct sun light, as a feasible option for next generation PVs. Concentrator PVs (CPVs) is a technology-agnostic approach toward increasing power conversion efficiency (PCE). In CPV configuration, sun-light is focused onto a small-area using lenses (or parabolic mirrors as concentrating optics[3]), which we illustrate in **Fig. 1**. The increased light intensity results in a higher density of photo-generated carriers, which drives a larger quasi fermi level splitting in the semiconductor absorber material (**Fig. 1d**), delivering a higher output voltage and hence increased power conversion efficiency of the cells[3]. Commercial CPVs are multi-junction cells based on III-V semiconductors[4,5]. To date, the record PCE of a CPV cell is 46% for a four-junction GaInP/GaAs/GaInAsP/GaInAs under 508 suns irradiance, whereas a similar 5-junction cell achieves 38.8% under one-sun illumination[6]. The reason that it has been feasible to employ the III-V multi-junction technology in CPV applications, is that the active cell area is small in comparison to the total area of the module capturing sun light, enabling the high cell cost to be accommodated in the overall cost of the deployed PV array [25]. However, this does set a significant demand upon, and hence cost of the solar tracking and concentrating optics, and an conflicting challenge to deliver a highly cost competitive CPV solution has arisen [25]. Presently, due to the continuing downward drive in the price for conventional PV, III-V multi-junction CPVs are struggling to compete with the same scale of growth which is occurring with flat-plate PV technologies[2].

Development of low-cost and high-efficiency materials for CPV applications, which could allow for less stringent solar tracking and concentrating optics, could therefore dramatically reset the cost competitive balance. In recent times, low-concentrator factors of the order of 10 to 100 fold have been experimented with for high efficiency silicon cells[2,7]. Thus far however, the cost balance has not made this favourable over conventional flat-plate deployment strategies, presumably due to the energy generation gains having not outweighed the additional costs. This therefore suggests that efficiencies greater that what is currently achieved with single junction Si PV, combined with cell costs which are not more expensive than Si, will be necessary in order to make the economics feasible for low-concentration factor CPV.

Photovoltaics based on metal halide perovskites have recently emerged as an interesting option for a technology which combines both high efficiency and low cost[8–10]. Single junction cells have achieved efficiencies of over 22%[11,12], and tandem cells constructed by combining perovskite top cells with silicon, have achieved efficiencies over 26%[13,14]. Beyond the performance already demonstrated in laboratories, we have recently estimated that it will be feasible for perovskite solar cells to surpass 38%

efficiency when measured under one-sun illumination, when integrated into a triple junction architecture[15]. We could therefore consider that by combining perovskite multi-junction cells with silicon PV and delivering much higher efficiencies, we may be able to tip the economics in favour of low-concentration CPV for large-scale deployment.

Perovskite solar cells are capable of sustaining linearity in the photocurrent generation up to many tens of sun intensity.[16–19] However, increased efficiency under increased light intensity is yet to be demonstrated. Another key consideration for CPV applications is the intrinsic material stability to intense sun light, where any light induced degradation is expected to be accelerated proportionally to the solar concentration factor. Despite early stability measurements on perovskite solar cells exhibiting fast degradation under one-sun illumination[20,21], recent advancements with perovskite composition and device architecture have led to significant improvements in long term operational stability[13,22,23] Furthermore, we have recently theoretically assessed the prospect of perovskite PV cells under high irradiance levels[24]. Based on kinetic considerations we have estimated that perovskite PVs should be capable of sustaining high efficiency under concentrated sun light. This collectively places perovskites in a very interesting space for consideration in low-concentration factor CPV applications.

Here, we experimentally assess a range of perovskite solar cells for both performance and stability under high intensity irradiance. We fabricate CPV devices based on different perovskite absorbers $APbX_3$; with the archetypal methylammonium (MA) A-site cation, mixed-cation formamidinium-cesium (FA/Cs) and triple-cation methylammonium-formamidinium-cesium (FA/MA/Cs) lead tri-(iodide-bromide) perovskites, and compare their device performance under a wide range of monochromatic light intensities. Through spectroscopic and thermogravimetric analysis, we also investigate the intrinsic material stability. We observe that the FA/Cs perovskite composition delivers the most stable perovskite cells under high irradiance. We find that these perovskite solar cells can perform well on most performance parameters up to 53 times equivalent solar concentration, with a continuous linear increase in short-circuit current density (J_{sc}) and a semi-logarithmic increase in open-circuit voltage (V_{oc}). However, they lose fill factor (FF) for intensities beyond 10-suns, which we identify to be primarily limited by the series resistance in the charge extraction layers. Importantly, we also demonstrate hundreds of hours of operational stability under 10-suns irradiance. Our proof-of-principle study demonstrates that metal halide perovskites should be considered as a serious option for low concentrator factor CPVs, and highlights key areas for further focus of research activities.

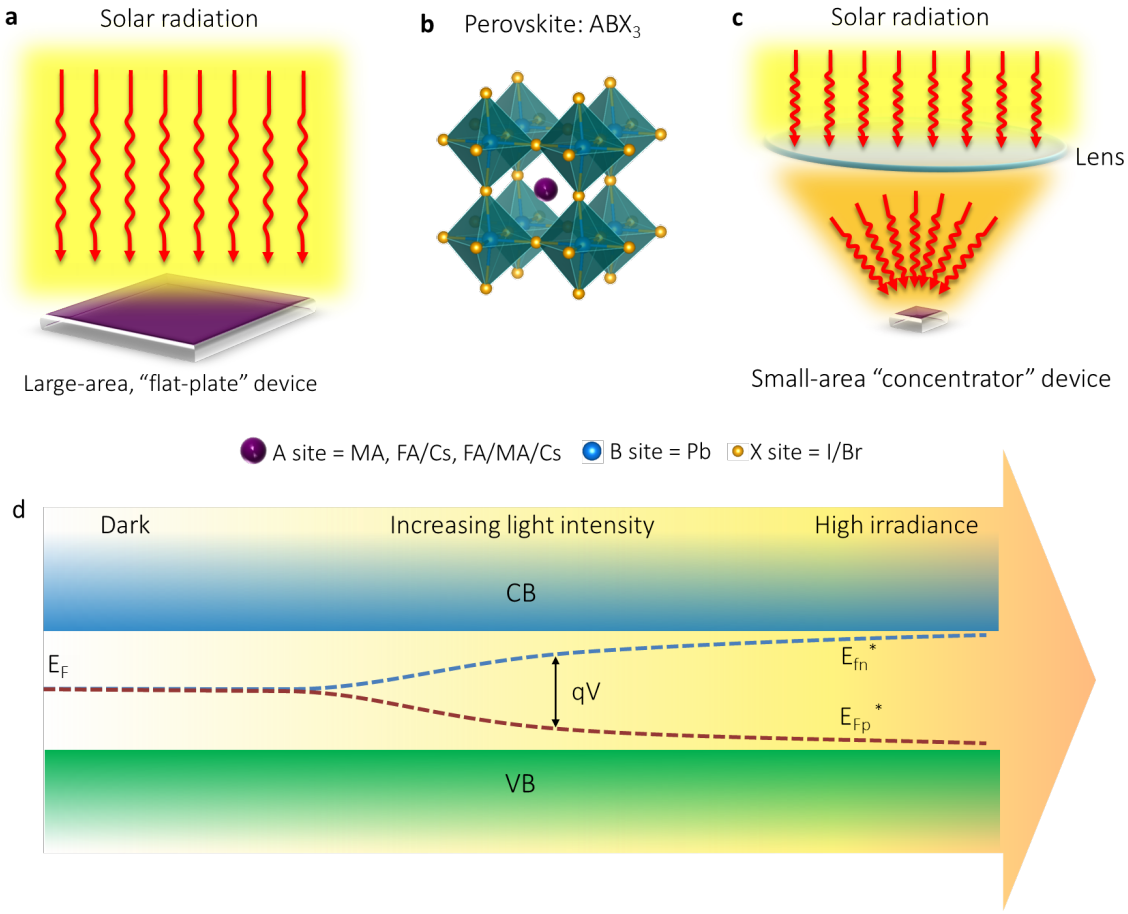

Figure 1. **Perovskite-based concentrator photovoltaics**. **a**, Large-area, 'flat-plate' perovskite solar cell devices operated up to 1 sun irradiance. **b**, ABX_3 perovskite crystal structure, the MA, FA and Cs stand for methylammonium ($CH_3NH_3^+$), formamidinium [$(NH_2)_2CH^+$] and caesium, respectively. **c**, Perovskite CPV devices. The normal 1-sun irradiance is concentrated onto a small-area perovskite solar cell by a focusing lens or a parabolic mirror (not shown here), which delivers a higher power output. **d**, Schematic illustration of the Fermi level splitting in a solar absorber material with increasing light intensity. E_F represents intrinsic fermi level. E_{Fn}^* and E_{Fp}^* are the quasi-Fermi levels for electrons and holes respectively, where light absorption results in electrons populating the conduction band (CB), and holes populating the valence band (VB).

Material stability.

We first investigated the fundamental stability under high irradiance of both thin films and devices comprising a range of different perovskite compositions, and present our results and associated discussion in **Supplementary Notes 1-3** and **Supplementary Figs. 1-6**. Form the materials we assessed, we find that $FA_{0.83}Cs_{0.17}PbI_{2.7}Br_{0.3}$ (FA/Cs) is the

most stable composition, and FA/Cs devices deliver the highest efficiency under high irradiance. We therefore focus on this FA/Cs composition for our CPV study here.

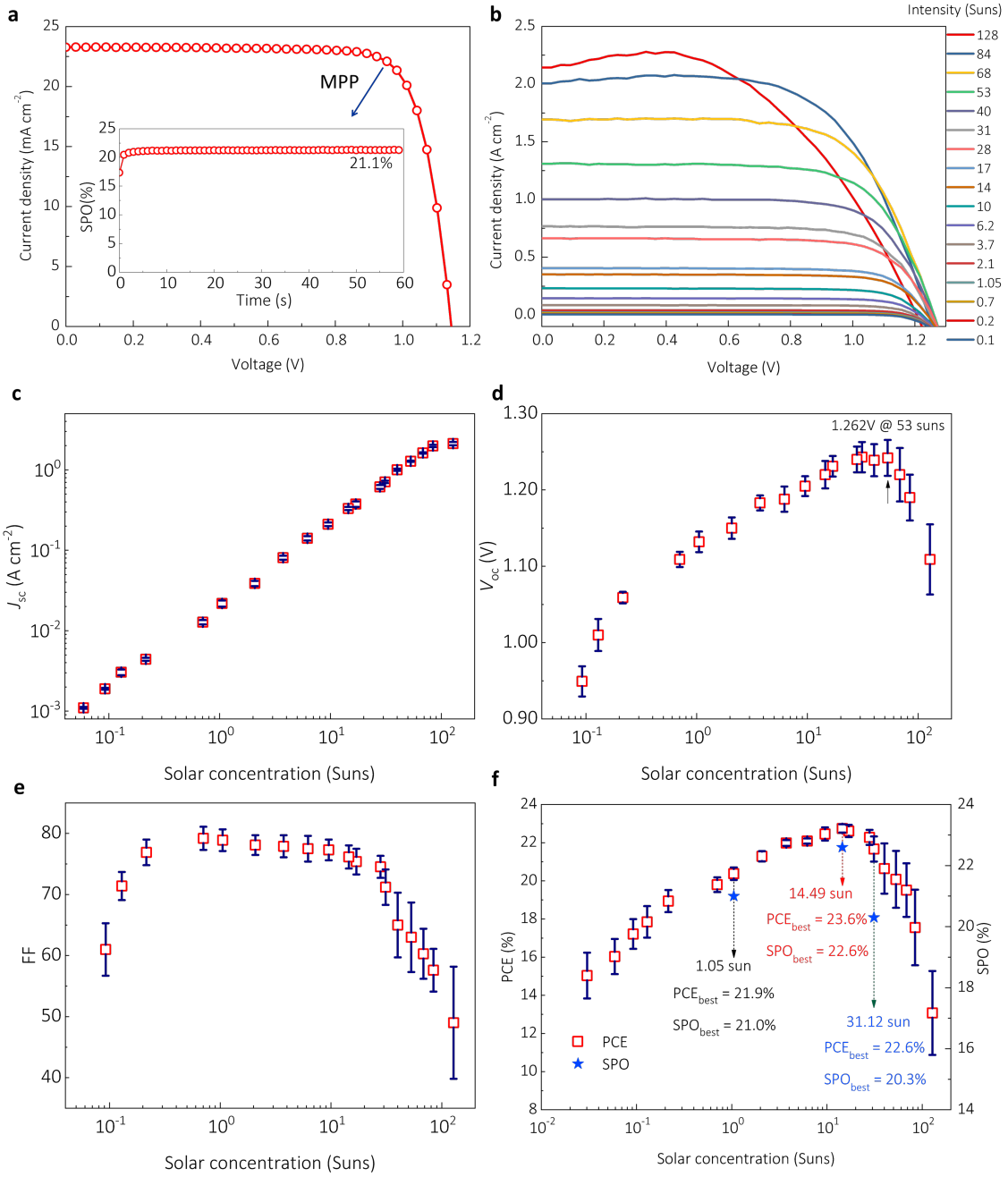

Figure 2. CPV device performances. a, *J–V* characteristic of a best performing FA/Cs perovskite solar cell with an optically masked active area of ~9.19 mm^2, measured under simulated AM1.5G solar irradiance at 100 mW cm^{-2} (*i.e.* 1 sun) with 2-wire connections under source mode. The inset shows the corresponding stabilized power output (SPO) data, determined by holding the cell at a fixed voltage near the maximum power point (MPP) on the *J–V* curve for 60 s. The cell structure is

glass/FTO/SnO_2/$FA_{0.83}Cs_{0.17}PbI_{2.7}Br_{0.3}$/spiro-OMeTAD/Au. **b**, Measured *J–V* characteristics of the champion device under simulated concentrated AM 1.5G sunlight at various irradiance levels. The active cell area was ~ 0.82 mm^2 for the devices measured under high irradiance, in order to reduce parasitic series resistance losses. **c-f**, Comparison of (**c**) J_{sc}, (**d**) V_{oc}, (**e**) FF, and (**f**) PCE of perovskite solar cell devices measured under various solar concentration factors (up to 128 suns). Each average (symbol) and standard deviation (error bar) was calculated from eight devices. The PCE_{best} and SPO_{best} values represent the highest scanned efficiency and stabilised efficiency, respectively, measured from the champion device. High intensity illumination was with an AM 1.5G filtered xenon lamp solar simulator with a parabolic reflector and neutral density filers employed to vary the irradiance levels (see spectrum in the **Supplementary Fig. 7**). All the light intensity measurements are performed on unsealed cells in ambient air under a 4-wire, source and sense mode.

CPV performance under concentrated sunlight.

We now inspect the CPV performance of the FA/Cs cell under simulated AM 1.5G full spectrum sunlight. The spectrum of the concentrated light source and concentrator setup are shown in **Supplementary Fig. 7 and 8**. We give more details of our measurement and spectral mismatch estimation in the experimental section. In **Fig. 2a** we show the *J-V* curve of the champion FA/Cs device measured under AM 1.5G 100 mW cm^{-2} irradiance (*i.e.* 1 sun) with a 2-wire connection under source mode. The device exhibits a J_{sc} of 23.2 mA cm^{-2}, a FF of 0.80, and a V_{oc} of 1.14 V, yielding a PCE of 21.1%. In **Supplementary Fig. 9**, we show the photovoltaic performance parameters extracted from *J-V* curves (**Fig. 2b**) measured via 4-wire source and sense mode, which overcomes resistive losses in the electrical cables, and contact resistance between the connecting pins. In **Fig. 2c-f** we show the statistics of photovoltaic characteristics of the entire device population under various concentrations. We observe a linear increase in the J_{sc} and a semi-logarithmic increase in the V_{oc} with increasing light intensity. Notably, the V_{oc} reaches a substantial value of 1.26 V at a high concentration of 53 suns. While the V_{oc} increases at a rate of 80 mV/decade, the main limitation remains the FF, but this does not start to significantly deteriorate until intensities above 10 suns. Nevertheless, we achieve a champion efficiency of 23.6% under 14 suns and 22.9% under 31 suns from a relatively stable FA/Cs perovskite solar cell.

Returning to the V_{oc}, we would expect the V_{oc} to increase monotonically with increasing charge carrier density within the perovskite film and never reduce with increasing light intensity.[25,26] We have recently theoretically assessed the fundamental limitations of $MAPbI_3$ perovskite solar cells under high irradiance. Simply based on the

spectroscopically derived recombination rates, and with assumptions about charge collection rates, we have estimated that the V_{oc} should continuously rise, and the efficiency should increase to over 100 suns irradiance. In order to verify that the perovskite absorber layer itself is not limiting the performance of our solar cells here under high irradiance, we consider the recombination processes occurring with the FA/Cs perovskite absorber: we know that at low charge carrier densities monomolecular processes dominate recombination. Under these conditions charge recombination occurs through traps, or to a background of doped carriers, with characteristic recombination rate constant k_1 and total recombination rate proportional to the charge density (n). At intermediate charge densities, band-to-band bimolecular processes dominated recombination, with characteristic rate constant k_2 and total rate proportional to n^2. Under high charge densities, 3rd order Auger process dominates recombination[27], with a characteristic rate constant of k_3 and the total rate proportional to n^3. With prior knowledge of these rate constants for the different perovskite absorber materials, which have been determined via spectroscopic studies, and by assuming steady state conditions at open-circuit, we can estimate the equivalent charge density, and the equivalent solar concentration factor (C), at which the transition between these different regimes will occur. In addition, knowing the total recombination rate and the charge carrier diffusion coefficient, we can estimate how the charge carrier diffusion length within the absorber layer should change with charge density and solar concentration factor. In **Fig. 3** we show the calculated charge carrier diffusion length plotted against charge carrier density, and indicate and tabulate the equivalent solar concentration factors at the transition between the different dominating modes for charge recombination for the MA and FA/Cs perovskites. We give a full description of our estimations in the **Supplementary Note 4** and **Supplementary Table 1**.

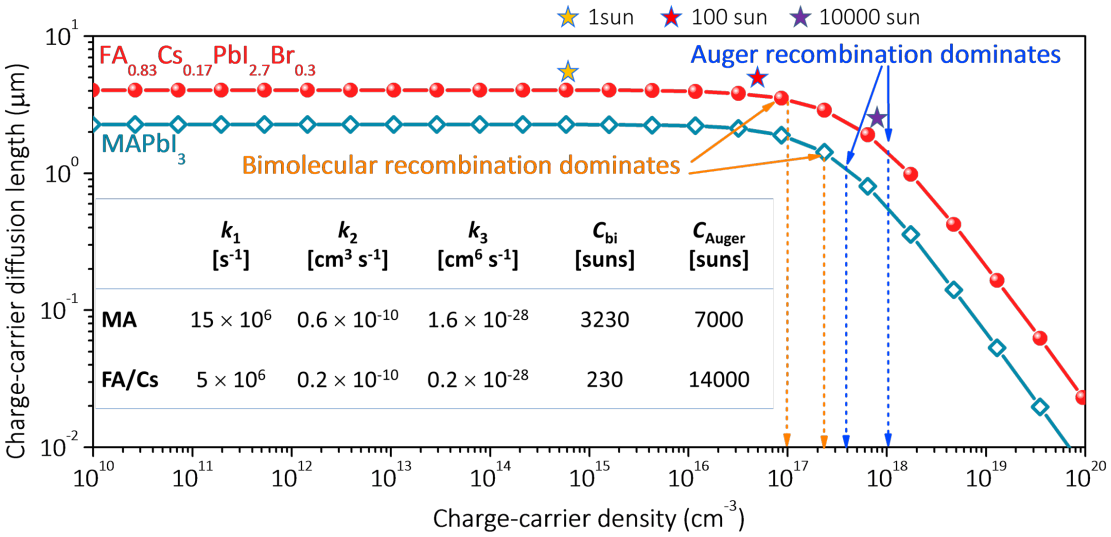

Figure 3. Charge carrier diffusion length and recombination processes. Calculated charge-carrier diffusion lengths as a function of charge-carrier density. The inset table shows the estimated equivalent solar light concentration when recombination is dominated by bi-molecular, (C_{bi}) and Auger (C_{Auger}) recombination. MA and FA/Cs stand for $MAPbI_3$ and $FA_{0.83}Cs_{0.17}PbI_{2.7}Br_{0.3}$, respectively. The monomolecular recombination rate constant (k_1), biomolecular recombination rate constant (k_2) and Auger recombination rate constant (k_3) of the MA and FA/Cs absorber layers are extracted from refs. [28] and [29], respectively. The star symbols represent the estimated equivalent solar concentration required to generate the corresponding charge carrier density for the FA/Cs perovskite.

As we show in **Fig. 3**, we determine that the recombination within the FA/Cs perovskite film should remain dominated by monomolecular processes up until around 230 suns, and bimolecular recombination should then dominate until Auger recombination dominates at concentrations above 14,000 suns. Additionally, for the FA/Cs perovskite, the charge carrier diffusion length remains greater than four microns until over 100 suns concentration, and over two micron until over 10,000 suns. Therefore, by simply considering the metal halide perovskite absorber layer, we would expect the perovskite solar cells to operate perfectly efficiently up to concentrations well beyond 1,000 suns.

Our estimations for diffusion length and carrier recombination processes are very encouraging for the potential use of perovskite absorbers in CPV, but do imply that our observed "saturation" and further reduction in V_{oc} with increasing light intensity must originate from other "non-perovskite" components of the cells, or changes to the perovskite absorber with increasing light intensity, such as increased trap density

(monomolecular recombination rate) or degradation. Importantly, in our measurements we start at low intensity and increase, and we observe that the V_{oc}–suns measurement at high irradiance is not reversible. We show a repetitive measurement of a cell under 142 suns in **Supplementary Fig. 10**, where we observe a progressive drop in J_{sc} and V_{oc}. Therefore, under the highest intensity light exposure in air, we are inducing a permanent degradation of the cells. We thus consider this intensity of peak V_{oc} to indicate a degree of photo-stability of the perovskite film and device in ambient conditions, rather than a fundamental limitation of electronic properties.

Traditionally, information about the "mode" of recombination can be gained from estimating the "ideality factor" of the solar cell. This is how closely the solar cell operational characteristics represent that expected from an electronic model of a single diode. A numerical factor - the ideality factor - is inserted in the diode equation, as we describe in **Supplementary Note 5**. This factor can carry some physical meaning, where an ideality factor of 1, traditionally implies that all recombination is proceeding via bimolecular recombination, and an ideality factor of 2, traditionally implies that all recombination is proceeding monomolecular via trap assisted recombination. According to our estimations above, we expect to be in the monomolecular regime over these intensity ranges, and we hence expect the ideality factor to be approximately 2. However, we estimate the ideality factor from the slope of the V_{oc} versus light intensity, and determine a value of 1.3. In addition, we estimate the ideality factor from fitting of the *J-V* curves, which we show in **Supplementary Fig. 11**. This figure shows a variable ideality factor which increases from less than 1 at low concentrations, to 4.5 at the highest concentrations. Notably ideality factors of greater than 2 have a non-physical meaning according to traditional theory. The origin of these apparently non-physical and variable ideality factors, is likely to arise from the combined presence of both mobile ions and traps in the perovskite semiconductors, part of the same mechanism which results in hysteresis in the JV curves of the perovskite solar cells[30,31]: Under different electrical bias and light exposure regimes, ions will migrate to different regions of the solar cells and either make the conditions favourable to stabilise filled traps near the surface of the perovskite absorber layer, or make the conditions favourable to induce rapid depopulation of traps. When the traps are mostly filled, we expect to have a smaller fraction of trap assisted recombination, longer charge diffusion lengths and an ideality factor closer to 1. When the traps are predominantly empty we expect to have a higher fraction of trap assisted recombination, shorter diffusion lengths, and a higher ideality factor. Recently, Barnes and co-workers have highlighted the challenges with ideality factor estimations, and suggest measuring the transient V_{oc} as a function of light intensity as a means to derive

the ideality factor[32]. Tress et al, have also estimated variable ideality factors for perovskite solar cells, and advocate fitting of dark JV measurements as a suitable methodology[33,36]. Clearly this aspect requires further investigation.

As we have discussed above, we do not expect limitations on charge extraction from the perovskite layer to set-in until solar concentrations beyond 1,000 suns. Therefore, this "FF roll-off" is likely to originate from either resistance from the charge extraction layers, contact resistance between the internal layers of the solar cell, or simply parasitic resistance in the fluorine doped tin oxide transparent conducting electrode (TCE), as has been previously observed for organic photovoltaics[34,35]. In order to disentangle the contributions to series resistance in our cells, we have performed measurements on the individual components, by measuring *J-V* curves of "sub-cells", which have the same architecture as the solar cells, but with many layers, including the perovskite absorber layer, missing. In the same manner as we employ for the solar cells, for all the sub-cells, we include an additional electrically conductive silver ribbon adhesive in order to minimize the series resistance for the charge conducted through the FTO to the gold metallic contact. The sub cells are FTO/Au, to estimate the series resistance in the FTO and metallic conductors, FTO/SnO_2/Au to estimate the additional series resistance contribution from the n-type charge collection layer, and FTO/spiro-OMeTAD/Au to estimate the series resistance contribution from the hole-conductor. The results are shown in **Supplementary Figure 12** and **Supplementary Table 2.** We find that the main resistance originates from the spiro-OMeTAD layer, and the combined contribution from the FTO, SnO_2 and spiro-OMeTAD add up to closely match the series resistance of the solar cell, as determined by the slope of the *J-V* curve at V_{oc}. Therefore, to improve the efficiency of our perovskite CPV devices further under higher irradiance levels, we need to find, in order of priority, charge extraction layers which have much lower series resistance than spiro-OMeTAD and SnO_2, and use higher conductivity TCOs or metallic grids for charge extraction.

Note that we did not actively cool the devices during the increase irradiance tests. We estimate the cell temperature during operation with an infrared camera, as we show in **Supplementary Fig. 13,** and measure the cell surface temperature to rise from 23 to 38 ˚C, over the course of a typical measurement. This increase in cell temperature will also contribute to the lower than expected V_{oc} at high irradiance levels, since V_{oc} drops with increasing temperature[36,37]. We have also found that the stability of this perovskite CPV device from prolonged exposure to high irradiance levels is poor, as shown in **Supplementary Fig. 14,** which we postulate to be limited by the instability introduced by employing spiro-OMeTAD hole transporting layer. To tackle this instability issue, we

optimize cells employing poly[bis(4-phenyl)(2,5,6-trimethylphenyl)amine (PTAA) as the hole transporting layer. Furthermore, we coat the SnO_2 compact layer with a thin layer of 4-(1,3-dimethyl-2,3-dihydro-1H-benzimidazol-2-yl)-*N*,*N*-diphenylaniline (*N*-DPBI) doped phenyl-C_{61}-butyric acid methyl ester ($PC_{61}BM$) to further enhance the device stability[22]. These "improved stability devices" have a structure of glass/FTO/SnO_2/$PC_{61}BM$/perovskite/PTAA/Au, which delivers close to comparative efficiency under 1 sun and higher irradiance, which we show in **Supplementary Figs. 15, 16 and 17**.

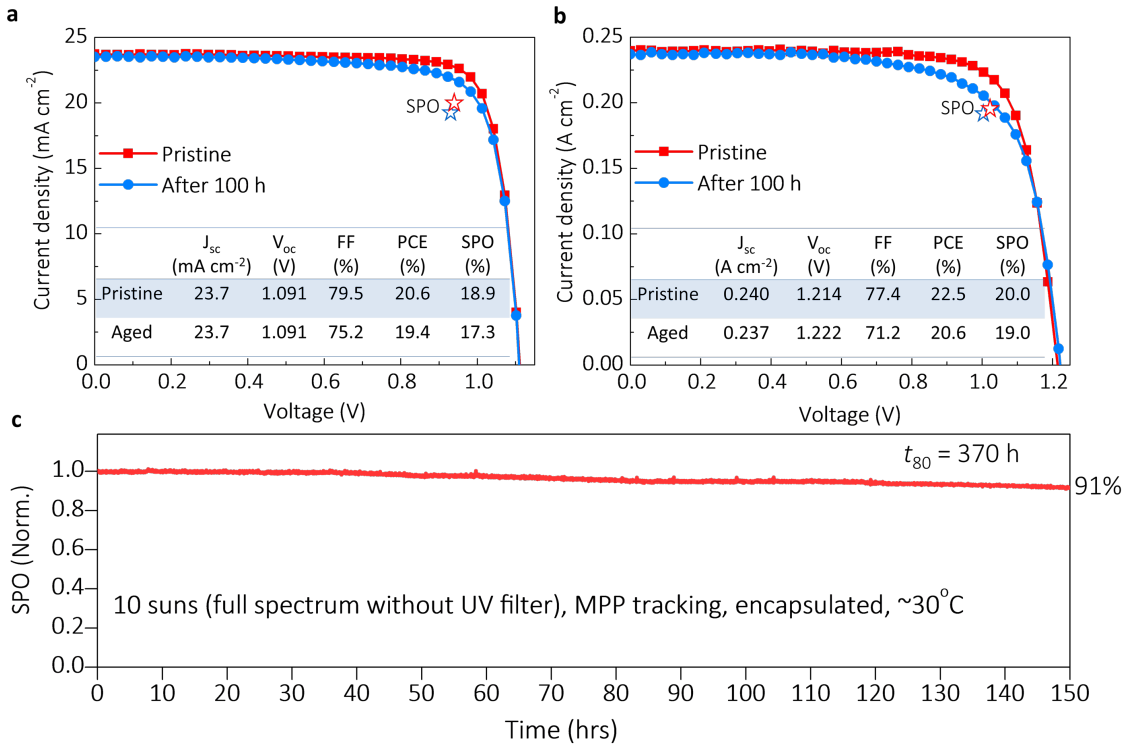

Figure 4. **CPV stability under concentrated light**. **a**,**b** *J*-*V* curves of the pristine and aged devices measured under 1 sun (**a**) and 10-suns irradiance (**b**). The insets give the JV curve performance parameters and the large star symbols show the SPO values. **c**, SPO of the perovskite devices, continuously recorded under 10 suns concentration. The device structure is FTO/SnO_2/PCBM/$FA_{0.83}Cs_{0.17}PbI_{2.7}Br_{0.3}$/PTAA/Au. Illumination was with a xenon lamp simulated full spectrum AM 1.5 G simulator (spectrum shown in **Supplementary Fig. 18**). The device is held at maximum power point (MPP) during aging and kept at a constant temperature by an air stream flowing onto the devices (FTO side), with the device surface measuring approximately 30 ºC. All measurements were performed on encapsulated cells in ambient air. The active cell area was ~1 mm^2.

To assess the stability of these devices under high irradiance, we measure the stabilized efficiency of the encapsulated solar cells glass/FTO/SnO_2/$PC_{61}BM$/perovskite (FA/Cs)/PTAA/Au solar cells by holding them at maximum power point (MPP) under concentrated sunlight (10 suns) and present the results in **Fig. 4**. We actively cooled the cell with flowing air from a compressed air source, which maintained the cell temperature at 30 ˚C. Very encouraging, we observe excellent stability under 10 suns irradiance, with the cell maintaining 91% of its original efficiency after 150 h. From the JV curves measured during the aging process (**Fig. 4a** and **b**), we determine that the degradation is mainly due to the drop in FF. We determine the lifetime to 80% degradation (t_{80}) at 10-suns irradiance to be 370 hrs.

Conclusion

In conclusion, we have experimentally demonstrated increased efficiency and substantial stability of perovskite solar cells under simulated concentrated solar irradiance. By comparing the structural, optical and optoelectronic properties of MA, FA/MA/Cs and FA/Cs perovskite films, we identify the FA/Cs perovskite as the most suitable, due to improved thermal stability and higher tolerance to high levels of irradiance. By employing the FA/Cs perovskite as a photoactive layer in a single-junction solar cell, we boost the PCE from 21.3% under 1 sun, to 23.6% under 14 suns irradiance. We have found that the key limiting factor with increasing irradiance is a deterioration of the FF at concentrations above 10 suns, which should be surmountable by future adaptations to reduce the series resistance contribution from the charge extraction layers. We note that the V_{oc} of a champion FA/Cs device reaches an impressive 1.26 V at 53 suns concentration, indicating the great potential of perovskite solar cell for CPV applications. Of critical importance, the FA/Cs device employing relatively stable interfacial layers sustains over 90% of its original efficiency after 150 h aging at 10 suns concentrated sunlight. We expect the material innovation and fast developments in the perovskite field of research to enable efficient and stable perovskite CPVs to be realised in the near future, which ultimately should employ perovskite tandem and triple junction cells to facilitate the maximum power conversion efficiency. Beyond strategies to further increase the efficiency, moving forward, there are four key areas we believe require significant scrutiny and further enhancements. First, reduction of the series resistance in the charge extraction layers to improve FF under high irradiance levels. Second, a better understanding of the present limitations and improvements to the long-term operational stability under high levels of irradiance and elevated temperatures. Third, adaptation of the cell design and thermal management strategies to enable the cells to operate at as low

a temperature as possible under concentrated sun light. Finally, development of strategies for the optical design of the concentrating optics, including macroscopic lenses, parabolic mirrors and micro-lenses, in order to achieve an economically viable deployable perovskite CPV technology under low-concentrated sunlight.

Methods

Preparation of perovskite films: $MAPbI_3$ solution: 1.2 M perovskite precursor solution was prepared using a 4:1 (v:v) mixed solvent from anhydrous DMF and DMSO (Sigma-Aldrich) with desired composition using precursor salts: methylammonium iodide (MAI; Dyesol), lead iodide (PbI_2; TCI). $FA_{0.83}Cs_{0.17}PbI_{2.7}Br_{0.3}$ solution: 1.45 M perovskite precursor solution was prepared using a 4:1 (v:v) mixed solvent from anhydrous DMF and DMSO (Sigma-Aldrich) with desired composition using precursor salts: formamidinium iodide (FAI; Dyesol), cesium iodide (CsI; Alfa Aesar), PbI_2 (TCI), lead bromide ($PbBr_2$; TCI). $FA_{0.7}MA_{0.25}Cs_{0.05}PbI_{2.7}Br_{0.3}$ solution: 1.45 M perovskite precursor solution was prepared using a 4:1 (v:v) mixed solvent from anhydrous DMF and DMSO (Sigma-Aldrich) with desired composition using precursor salts: FAI (Dyesol), MAI (Dyesol), CsI (Alfa Aesar), PbI_2 (TCI), $PbBr_2$ (TCI). All solutions were prepared in a nitrogen-filled glovebox and kept stirring overnight at room temperature. The $MAPbI_3$ films were deposited through a two-step spin coating program (10 s at 1000 rpm and 15 s at 5000 rpm) with dripping of anisole (Sigma-Aldrich) as anti-solvent during the second step, 10 s before the end. The films were then transferred to a hotplate immediately and annealed at 100 °C for 10 min. For the FA/Cs and FA/MA/Cs perovskite films, the precursor solutions were spin-coated through a two-step spin coating program (10 s at 1000 rpm and 35 s at 6000 rpm) with dripping of anisole (Sigma-Aldrich) as anti-solvent during the second step, 10 s before the end. The films were then annealed at 100 °C for 60 min. All films were spin-coated in a drybox with relative humidity below 20%.

X-ray diffraction: All XRD Spectra were obtained on a Rigaku SmartLab X-ray diffractometer with $CuK_{\alpha 1}$ (1.54060 Å) and a HyPix-3000 2D hybrid pixel array detector, and operated at 40 kV with a 2θ scan range of 10–30°.

Thermogravimetric (TGA) analysis: We first deposited perovskite films on glass substrates using the same procedure for device fabrication. Then we scratched the well-crystallized perovskite films from the glass substrate and collected the perovskite powders for the TGA measurement. TGA was carried out in open ceramic pans under a

constant flow of nitrogen at 200 ml min^{-1} using a Perkin Elmer TG/DTA. Each sample was heated from room temperature to 800˚C under nitrogen using a scan rate of 10˚C/min.

Photoluminescence measurement: The PL spectra were collected with an intensified charge coupled device (iCCD, PI-MAX4, Princeton Instruments), photoexcited by a 400 nm laser operated at continuous wave (CW) mode with a fluence of ~790 mW cm^{-2}– calibrated with a power meter, which generates equivalent carrier density with 10 suns irradiance of white light. More details about the conversion of equivalent power are described later.

Fabrication of perovskite solar cell devices: For the electron-transporting layer, 0.05 M $SnCl_4 \cdot 5H_2O$ (Sigma-Aldrich) was first dissolved in anhydrous isopropanol and stirred for 30 min at room temperature. The solution was deposited on cleaned FTO substrates with 3000 rpm spin rate for 30 s, followed by pre-drying at 100 ^oC for 10 min and then heat-treated at 180 ^oC for 1 h. The films were then treated using chemical bath deposition method, as described somewhere else[38]. 500 mg urea (Sigma-Aldrich) was dissolved in 40 ml deionized water, followed by the addition of 10 ml mercaptoacetic acid (Sigma-Aldrich) and 0.5 ml HCl (37 wt%). Finally, $SnCl_2 \cdot 2H_2O$ (Sigma-Aldrich) was dissolved in the solution at 0.002 M and stirred for 2 min. The deposition was made by putting the substrates in a glass Petri dish filled with the above solution, in a 70 ^oC lab oven for 3 h. The treated substrates were rinsed in a sonication bath of deionized water for 2 min, dried in a stream of nitrogen and annealed for 1 h at 180 ^oC. For the stability test, we further add a layer of doped $PC_{61}BM$: we dissolve $PC_{61}BM$ (Solenne) in anhydrous 1,2-dichlorobenzene (DCB; Sigma-Aldrich) at 10 mg ml^{-1}. We dissolve the dopant 4-(1,3-dimethyl-2,3-dihydro-1H-benzimidazol-2-yl)-*N,N*-diphenylaniline (*N*-DPBI; Sigma-Aldrich) dissolved in DCB at 10 mg ml^{-1}. Both of the PCBM and *N*-DPBI solutions were stirred overnight at room temperature. Prior to deposition, we add 20 μl of *N*-DPBI solution in 1 ml PCBM precursor solution. Then, we spin coat the doped PCBM solution on top of the as-prepared SnO_2 layer in a nitrogen-filled glovebox at 2500 rpm for 40 s, and annealed in nitrogen at 80 ^oC for overnight to achieve successful doping. More details are reported elsewhere[22].

For the perovskite absorber layer, we use same protocols as the thin film fabrication.

For the 2,20,7,70-tetrakis[*N,N*-di(4-methoxyphenyl)amino]-9,90-spirobifluorene (spiro-OMeTAD) hole transporting layer, to obtain a spiro-OMeTAD solution, we dissolved 85.7 mg spiro-OMeTAD (Borun Technology) in 1ml anhydrous

chlorobenzene with additives of 28.8 ul tert-butylpyridine (*t*BP) and 20 ul lithium bis(trifluoromethylsulfonyl)imide (Li-TFSI) salt in acetonitrile (520 mg ml^{-1}). For the poly[bis(4-phenyl)(2,5,6-trimethylphenyl)amine (PTAA) hole-transporting layer, to obtain a PTAA solution, we dissolved 10 mg PTAA (Flexink) in 1ml anhydrous chlorobenzene. Tris(pentafluorophenyl)borane (Sigma-Aldrich) was dissolved in anhydrous chlorobenzene and mixed with PTAA at a ratio of 20 mol%. After the perovskite films cooled down to room temperature, the spiro-OMeTAD was spin-coated on the perovskite layer at 2,500 r.p.m. for 40 s in a dry box (<15 RH%) as a hole-transporting layer. We note that when employing the PTAA as a hole-transporting layer, we further spin coat a *t*BP solution (33 ul of *t*BP in 1 ml of chlorobenzene) on perovskite films at 4000 rpm for 30 s and annealed at 100 ºC for 10 min, prior to the PTAA deposition. Then, the PTAA solution was spin coated at 2,500 r.p.m. for 40 s in a dry box (<15 RH%).

For the electrode deposition, 100 nm gold electrodes were thermally evaporated under vacuum of ~5×10^{-6} Torr, at a rate of ~ 1 Å s^{-1}. Note that the temperature of the vacuum chamber was controlled under 35 °C during the evaporation of metal electrode, a higher temperature will cause possible degradation of perovskite films.

Current−Voltage measurements under AM 1.5G sunlight: The *J-V* curves were measured (2400 Series SourceMeter, Keithley Instruments) under simulated AM 1.5G sunlight at 100 mW cm^{-2} irradiance generated by an Abet Class AAB sun 2000 simulator, with the intensity calibrated with an NREL calibrated KG3 filtered Si reference cell. The mismatch factor was calculated to be less than 5%, and applied to calibrate the AM 1.5 G 100 mW cm^{-2} equivalent irradiance. The active area of the solar cell measured under AM 1.5 G is 9.19 mm^{-2}, defined by an opaque aperture mask. For the cells measured under simulated concentrated sun light, the cell area was mechanically scribed down to ~1 mm^2 in order to reduce series resistance in the FTO. In order to determine the active area of the small cell, we measured the unmasked small cells under AM 1.5 G illumination and matched the J_{sc} measured with the same cell prior to scribing, measured through the 0.0919 cm^{-2} aperture mask. This enabled us to measure the small area cells unmasked, without inducing significant errors from estimations of small masking areas, and difficult to quantify shading losses. The forward *J–V* scans were measured from forward bias to short-circuit and the backward scans were from short-circuit to forward bias, both at a scan rate of 380 mV s^{-1}. A stabilisation time of 5 s at forward bias of 1.4 V under illumination was done prior to scanning.

Current−Voltage measurements under concentrated sunlight: To avoid the effect of

parasitic resistance, the active area of the perovskite solar cells was reduced to ~ 1 mm^2. The concentrated light source was obtained via focusing a Xenon lamp simulated white light source including an AM 1.5G filter. The light intensity was modulated by a set of neutral density filters and the irradiance was determined using a KG3 filtered silicon reference cell and accounting for spectral mismatch, as described in the **Supplementary Note 6**. In order to set the "1 sun intensity", the perovskite test cell was used for self-calibration between the AAA class simulator and the concentrated solar simulator. To quantify the intensity on the concentrated solar simulator, at near 1-sun intensity, the J_{sc} was measured on the test cell and compared to the J_{sc} measured on the same cell, under the mismatch factor corrected AAA class AM 1.5G 100$mWcm^{-2}$ solar simulator. The *J-V* curves were recorded with a 2400 Series source meter (Keithley Instruments) via a four-wire connection mode, which overcomes resistive losses in the electrical cables, and contact resistance between the connecting pins.

Stability test: For stability measurement, the perovskite devices were encapsulated with UV adhesive (LT-U001, Lumtec) and a glass coverslip as a barrier layer in a nitrogen filled glove box. Before encapsulation, we blow the devices with nitrogen gun to remove any contaminations and stored them in a nitrogen-filled glovebox for overnight to remove any moisture residuals. The devices were aged at maximum power point under concentrated full spectrum simulated AM 1.5 G, 100 mA cm^{-2} irradiance. The device was constantly cooled by blasting compressed air stream onto the devices (FTO side) with the device surface measuring approximately 30^{o}C. We do not have control on the humidity but monitored the lab humidity, which ranged from 40 to 50% relative humidity at room temperature, during the course of the aging.

Data Availability. The data that support the plots within this paper and other findings of this study are available from the corresponding author upon reasonable request.

References

1. More than half of utility-scale solar photovoltaic systems track the sun through the day. (2017). Available at: https://www.eia.gov/todayinenergy/detail.php?id=30912.
2. Wiesenfarth, M., Philipps, S. P., Bett, , A. W., Horowitz, K. & Kurtz, S. *Current Status of Concentrator Photovoltaic (CPV) Technology*. *National Renewable Energy Laboratory* (2017).
3. Apostoleris, H., Stefancich, M. & Chiesa, M. Tracking-integrated systems for

concentrating photovoltaics. *Nat. Energy* **1,** 16018 (2016).
4. Dahal, R., Li, J., Aryal, K., Lin, J. Y. & Jiang, H. X. InGaN/GaN multiple quantum well concentrator solar cells. *Appl. Phys. Lett.* **97,** (2010).
5. Cotal, H. *et al.* III–V multijunction solar cells for concentrating photovoltaics. *Energy Environ. Sci.* **2,** 174–192 (2009).
6. Green, M. A. *et al.* Solar cell efficiency tables (version 50). *Prog. Photovoltaics Res. Appl.* **25,** 668–676 (2017).
7. Varieras, R. V., Wang, J. & King, D. L. System performance considerations for low-concentration linear-focus silicon-based photovoltaic modules. *IEEE J. Photovoltaics* **3,** 1409–1414 (2013).
8. Kojima, A., Teshima, K., Shirai, Y. & Miyasaka, T. Organometal halide perovskites as visible-light sensitizers for photovoltaic cells. *J. Am. Chem. Soc.* **131,** 6050–6051 (2009).
9. Lee, M. M., Teuscher, J., Miyasaka, T., Murakami, T. N. & Snaith, H. J. Efficient hybrid solar cells based on meso-superstructured organometal halide perovskites. *Science* **338,** 643–7 (2012).
10. Kim, H.-S. *et al.* Lead iodide perovskite sensitized all-solid-state submicron thin film mesoscopic solar cell with efficiency exceeding 9%. *Sci. Rep.* **2,** 591 (2012).
11. http://www.nrel.gov/ncpv/images/efficiency_charg.jpg. NREL efficiency chart. Available at: chart.jpg,. (Accessed: 16th June 2018)
12. Yang, W. S. *et al.* Iodide management in formamidinium-lead-halide–based perovskite layers for efficient solar cells. *Science (80-.).* **356,** 1376–1379 (2017).
13. Bush, K. A. *et al.* 23.6%-Efficient Monolithic Perovskite/Silicon Tandem Solar Cells with Improved Stability. *Nat. Energy* **2,** 17009 (2017).
14. Duong, T. *et al.* Rubidium Multication Perovskite with Optimized Bandgap for Perovskite-Silicon Tandem with over 26% Efficiency. *Adv. Energy Mater.* **7,** 1700228 (2017).
15. Hörantner, M. T. *et al.* The Potential of Multijunction Perovskite Solar Cells. *ACS Energy Lett.* **2,** 2506–2513 (2017).
16. Zhou, Y. & Gray-Weale, A. A numerical model for charge transport and energy convention of perovskite solar cells. *Phys. Chem. Chem. Phys.* **18,** 4476–4486 (2015).
17. Adhikari, K. R., Gurung, S., Bhattarai, B. K. & Mari, B. Dependence of perovskite solar cells performance on temperature and solar irradiation. *2015 3rd Int. Renew. Sustain. Energy Conf.* 1–6 (2015). doi:10.1109/IRSEC.2015.7455146
18. Leong, W. L. *et al.* Identifying Fundamental Limitations in Halide Perovskite

Solar Cells. *Adv. Mater.* **28,** 2439–2445 (2016).
19. Law, C. *et al.* Performance and stability of lead perovskite/TiO2, polymer/PCBM, and dye sensitized solar cells at light intensities up to 70 suns. *Adv. Mater.* **26,** 6268–6273 (2014).
20. Leijtens, T. *et al.* Overcoming ultraviolet light instability of sensitized TiO_2 with meso-superstructured organometal tri-halide perovskite solar cells. *Nat. Commun.* **4,** 2885 (2013).
21. Conings, B. *et al.* Intrinsic Thermal Instability of Methylammonium Lead Trihalide Perovskite. *Adv. Energy Mater.* **5,** 1500477 (2015).
22. Wang, Z. *et al.* Efficient and Air-Stable Mixed-Cation Lead Mixed-Halide Perovskite Solar Cells with n-Doped Organic Electron Extraction Layers. *Adv. Mater.* **29,** 1604186 (2017).
23. Wang, Z. *et al.* Efficient and ambient-air-stable solar cells with 2D-3D hetero-structured butylammonium-caesium-formamidinium lead halide perovskites. *Nat. Energy* **2,** 17135 (2017).
24. Lin, Q., Wang, Z., Snaith, H. J., Johnston, M. B. & Herz, L. M. Hybrid Perovskites: Prospects for Concentrator Solar Cells. *Adv. Sci.* **5,** 1700792 (2018).
25. Tress, W. Perovskite Solar Cells on the Way to Their Radiative Efficiency Limit - Insights Into a Success Story of High Open-Circuit Voltage and Low Recombination. *Adv. Energy Mater.* **7,** 1602358 (2017).
26. Saygili, Y. *et al.* Planar Perovskite Solar Cells with High Open-Circuit Voltage Containing a Supramolecular Iron Complex as Hole Transport Material Dopant. *ChemPhysChem* **19,** 1–9 (2018).
27. Herz, L. M. Charge-Carrier Mobilities in Metal Halide Perovskites: Fundamental Mechanisms and Limits. *ACS Energy Lett.* **2,** 1539–1548 (2017).
28. Milot, R. L., Eperon, G. E., Snaith, H. J., Johnston, M. B. & Herz, L. M. Temperature-Dependent Charge-Carrier Dynamics in CH3NH3PbI3 Perovskite Thin Films. *Adv. Funct. Mater.* **25,** 6218–6227 (2015).
29. Rehman, W. *et al.* Photovoltaic mixed-cation lead mixed-halide perovskites: links between crystallinity, photo-stability and electronic properties. *Energy Environ. Sci.* **10,** 361–369 (2017).
30. Van Reenen, S., Kemerink, M. & Snaith, H. J. Modeling Anomalous Hysteresis in Perovskite Solar Cells. *J. Phys. Chem. Lett.* **6,** 3808–3814 (2015).
31. Calado, P. *et al.* Evidence for ion migration in hybrid perovskite solar cells with minimal hysteresis. *Nat. Commun.* **7,** 13831 (2016).
32. Calado, P., Burkitt, D., Ya, J., Troughton, J., Watson, T.M., Carnie,

M.J., Telford, A.M., O'Regan, B.C., Nelson, J., Barnes, P. R. F. Identifying dominant recombination mechanisms in perovskite solar cells by measuring the transient ideality factor. *ArXiv* 1804.09049 (2018). doi:10.1111/gcb.14148

33. Tress, W. *et al.* Interpretation and evolution of open-circuit voltage, recombination, ideality factor and subgap defect states during reversible light-soaking and irreversible degradation of perovskite solar cells. *Energy Environ. Sci.* **11,** 151–165 (2018).
34. Manor, A., Katz, E. A., Tromholt, T., Hirsch, B. & Krebs, F. C. Origin of size effect on efficiency of organic photovoltaics. *J. Appl. Phys.* **109,** (2011).
35. Tromholt, T., Katz, E. A., Hirsch, B., Vossier, A. & Krebs, F. C. Effects of concentrated sunlight on organic photovoltaics. *Appl. Phys. Lett.* **96,** (2010).
36. Han, X., Qu, J. & Guo, Y. Dependence of silicon concentrator solar cells parameters on temperature and light intensity. *Taiyangneng Xuebao/Acta Energiae Solaris Sin.* **36,** 1585–1590 (2015).
37. Hörantner, M. T. & Snaith, H. Predicting and Optimising the Energy Yield of Perovskite-on-Silicon Tandem Solar Cells under Real World Conditions. *Energy Environ. Sci.* **10,** 1983–1993 (2017).
38. Anaraki, E. H. *et al.* Highly efficient and stable planar perovskite solar cells by solution-processed tin oxide. *Energy Environ. Sci.* **9,** 3128–3134 (2016).

Acknowledgement

This project has received funding from the European Union's Horizon 2020 research and innovation programme under grant agreement No 763977of the PerTPV project, and AFOSR through project FA9550-15-1-0115. B.W. acknowledges the European Commission for Marie Skłodowska-Curie actions individual fellowship (REA grant number: 706552-APPEL).

Author contributions

Z.W., Q.L. and H.J.S. conceived of the project. Z.W. designed the experiments, fabricated the devices and thin film samples. Z.W. performed the TGA, XRD measurement and analysed the data. Q.L. carried out photoluminescence and EQE measurements. Z.W. and Q.L. performed light intensity measurements. B.W. and M. G. C. helped with light intensity and four-wire measurements. Y.L. contributed to hole-transporting layer deposition. M.T.K. performed spectral mismatch corrections. L.M.H. and M.B.J. supervised the optical spectroscopy experiments. H.J.S. supervised the whole project.

Z.W. wrote the first draft of the paper. All authors discussed the results and contributed to the writing of the paper. †Z.W. and Q.L. contribute equally to this work.

Additional information

Correspondence and request for materials should be addressed to henry.snaith@physics.ox.ac.uk.

Competing interests

HJS is a co-founder and CSO of Oxford PV Ltd., a company commercialising perovskite PV technologies.